Experimental and numerical investigation into the drag performance of dimpled surfaces in a turbulent boundary layer

van Campenhout, O. W.G.; van Nesselrooij, M.; Lin, Y. Y.; Casacuberta, J.; van Oudheusden, B. W.; Hickel, S.

DOI
10.1016/j.ijheatfluidflow.2023.109110

Publication date
2023

Document Version
Final published version

Published in
International Journal of Heat and Fluid Flow

International Journal of Heat and Fluid Flow 100 (2023) 109110

Contents lists available at ScienceDirect

International Journal of Heat and Fluid Flow

journal homepage: www.elsevier.com/locate/ijhff

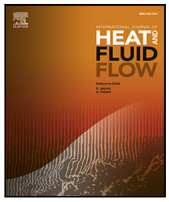

Experimental and numerical investigation into the drag performance of dimpled surfaces in a turbulent boundary layer

O.W.G. van Campenhout [a,b,*], M. van Nesselrooij [a,b], Y.Y. Lin [a], J. Casacuberta [a], B.W. van Oudheusden [a], S. Hickel [a]

[a] Aerodynamics Group, Faculty of Aerospace Engineering, TU Delft, Kluyverweg 1, 2629 HS Delft, The Netherlands
[b] Dimple Aerospace B.V., Kluyverweg 1, 2629 HS Delft, The Netherlands

ARTICLE INFO

Keywords:
Dimpled surface
Drag reduction
Turbulent boundary layer
Wind tunnel experiment
Large-eddy simulation

ABSTRACT

Although several previous studies have reported a potential drag-reducing effect of dimpled surfaces in turbulent boundary layers, there is a lack of replicability across experiments performed by different research groups. To contribute to the dialogue, we scrutinize one of the most studied dimple geometries reported in the literature, which has a dimple diameter of 20 mm and a depth of 0.5 mm. There is no general consensus in literature on the drag-reduction performance of this particular dimple geometry, with some studies suggesting a drag reduction, while others report a drag increase. The present combined experimental and numerical study comprises two sets of wind tunnel experiments and a well-resolved large-eddy simulation. The wind tunnel experiments and the large-eddy simulation both depict a total drag increase of around 1%–2% compared to the flat reference case. This finding agrees with a recent study by Spalart et al. (2019). Furthermore, the present wind tunnel experiments have shed light on a plausible reason behind the discrepancy between the study by Spalart et al. (2019) and earlier results from van Nesselrooij et al. (2016). Lastly, the large-eddy simulation results reveal that the pressure drag is the main contributor to the increase in the total drag of the dimpled surface. We believe that these results will contribute to a new consensus on the drag performance of this dimple geometry.

1. Introduction

The dimpled surface is a passive flow control technique introduced for heat transfer enhancement. However, this flow control technique has also been studied with the perspective to reduce turbulent skin friction at a limited increase of the pressure drag. Although this geometry has been studied since the 1970s, there is nevertheless no general consensus regarding its drag-reducing performance. One of the common denominators in the disagreement around dimpled surfaces has been the lack of replicability across independent experiments. In this article, drag performance is defined as the combined effect on the streamwise component of the integral of all stresses acting on the surface of the body, including tangential stresses (i.e., skin friction drag) as well as normal stresses (i.e., pressure drag).

Research on drag reduction in turbulent boundary layers by means of dimpled surfaces started during the 1970s in the Soviet Union. A group of scientists by accident found a lower pressure drop in a cooling system fitted with shallow dimples (Kiknadze et al., 1984). Ever since this discovery, various studies have been performed with these surfaces, leading to contradictory results. Some studies have reported a drag reduction (Veldhuis and Vervoort, 2009; Tay et al., 2015; van Nesselrooij et al., 2016) while others have found a drag increase (Lienhart et al., 2008; van Campenhout et al., 2018; Razzak et al., 2022). According to Gattere et al. (2022), a key challenge in assessing the results is a lack of replicability between the various studies. Lienhart et al. (2008) have tested geometries directly provided by Kiknadze et al. (1984), the scientists behind the original discovery. However, their study did not reproduce a drag reduction. van Nesselrooij et al. (2016) have tested the geometries inspired by Kiknadze et al. (1984), Veldhuis and Vervoort (2009), and Tay et al. (2015) but did not find a drag reduction over the geometries that did reduce the drag in the referred studies. The study by van Nesselrooij et al. (2016) did, however, find a ~4% drag reduction over a novel dimple geometry. When replicating these experiments, van Campenhout et al. (2018) found instead a marginal drag increase of ~1% for the same wind tunnel plate model.

Recently, Spalart et al. (2019) have performed an experimental and numerical study to assess the drag performance of the geometry that reduced the drag in the study by van Nesselrooij et al. (2016). Spalart

* Corresponding author at: Aerodynamics Group, Faculty of Aerospace Engineering, TU Delft, Kluyverweg 1, 2629 HS Delft, The Netherlands.
E-mail address: o.w.g.vancampenhout@tudelft.nl (O.W.G. van Campenhout).

https://doi.org/10.1016/j.ijheatfluidflow.2023.109110
Received 10 November 2022; Received in revised form 6 January 2023; Accepted 9 January 2023
Available online 18 January 2023

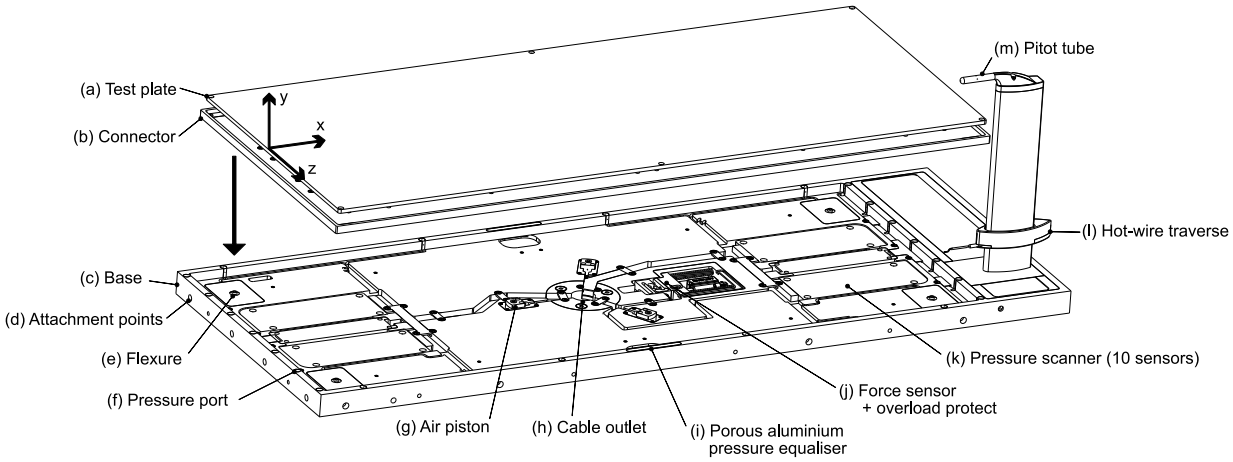

Fig. 1. Overview of the core elements of the novel measurement setup by van Nesselrooij et al. (2022). *Source:* Reprinted from van Nesselrooij et al. (2022) under the terms of the Creative Commons Attribution 4.0 license.

et al. (2019) report results for a direct numerical simulation (DNS) and a wind tunnel experiment. Both methods have shown the dimpled surface to increase the drag by ∼1% compared to the flat reference case. The wind tunnel experiment in the study by Spalart et al. (2019) is based on a wind tunnel setup and methodology that has been validated by Walsh (1982) for earlier studies on riblets. Spalart et al. (2019) found no justification for the inconsistency with the results from van Nesselrooij et al. (2016) and argued that "the situation is unsettled" given the discrepancy in drag performance. Further wind tunnel experiments are deemed relevant to investigate the differences between the results reported by Spalart et al. (2019) and van Nesselrooij et al. (2016). Furthermore, novel simulations are deemed relevant to replicate and strengthen the conclusions from Spalart et al. (2019) and to eventually resolve the discussion regarding the inconsistencies between different investigations.

The present article is intended as a direct response to the work of Spalart et al. (2019). Regarding the simulation of turbulent flow over dimpled surfaces, the authors of this article feel that one sensitive issue needs to be taken into account carefully. That is, there might be an influence of the relatively small numerical domain combined with streamwise periodic boundary conditions used by Spalart et al. (2019). Although the authors of this article have been in personal contact with Spalart regarding the results and methodologies of their investigation, this study has been based solely on the information published in their journal article.

This article is organized as follows: the experimental and numerical methodology is outlined in Section 2, the wind tunnel results are presented in Section 3, and the numerical results are analyzed in Section 4. Lastly, the synthesis of the numerical and experimental results is given in Section 5, followed by concluding remarks and an outlook in Section 6.

2. Methodology

2.1. Experimental methodology

Two different wind tunnel measurement setups are considered in this article: the improved experimental flat plate drag measurement setup from van Nesselrooij et al. (2022), and, in addition, the original setup used in van Nesselrooij et al. (2016), which has been rebuilt to investigate in particular the discrepancies between the results from van Nesselrooij et al. (2016) and Spalart et al. (2019). All measurements were performed in the so-called M-tunnel at Delft University of Technology. This low-speed wind tunnel has a cross-section of 400 mm × 400 mm and can reach flow speeds up to 32 m/s at which it has an inflow turbulence intensity of ∼0.7%.

2.1.1. Novel setup by van Nesselrooij et al. (2022)

An overview of the novel measurement setup by van Nesselrooij et al. (2022) and a definition of the core elements of the setup is given in Fig. 1. The measurement setup consists of three key elements: the test plate model with a dimension of 881.3 mm × 366.3 mm × 5 mm (item (a) in Fig. 1), the connector which provides the interface between the base and the freely moving test plate model (item (b) in Fig. 1), and the base structure with a dimension of 1020 mm × 395 mm × 30 mm which is connected directly to the wind tunnel (item (c) in Fig. 1). The test plate model is connected through the connector to a ± 2 N force sensor (item (j) in Fig. 1). Titanium flexures (item (e) in Fig. 1) allow the test plate model to swing with minimal drag in the direction of the freestream flow.

An important aspect of the setup is the implementation of a correction for the pressure forces acting on the streamwise-facing surfaces of the connector. Pressure variations in the gap between the connector and the base will also be registered by the force sensor as drag. For this reason, 15 pressure ports (item (f) in Fig. 1) have been added to the setup, which are used to correct for the pressure variations in the gap acting on the streamwise-facing surfaces of the connector.

This wind tunnel setup is capable of measuring differences in flat plate drag on the order of a few percent with sufficient confidence. Typically, the 95% confidence interval is less then 1% C_D, and often it is less then 0.5% C_D. Particularly, van Nesselrooij et al. (2022) calculate that measurements with this novel setup have four times less uncertainty compared to the measurements by Spalart et al. (2019). Further details on the setup, manufacturing methods, scrutinizing validation measurements, and measurement methodology can be found in the article by van Nesselrooij et al. (2022).

Seven plate models have been manufactured. These are the same designs as have previously been utilized in the original 2016 study. The plate models are denoted as plate models A to G and parametrized by five parameters, which are defined in Figs. 2 and 3. The corresponding parameters for the seven plate models are summarized in Table 1. Plate model A was reported to reduce the drag by ∼4% in the original 2016 study, while it increased the drag by ∼1% in the later study by Spalart et al. (2019).

2.1.2. Setup from van Nesselrooij et al. (2016)

For the replication of the 2016 experiments, the original setup used by van Nesselrooij et al. (2016) has been rebuilt. A schematic overview of the setup is given in Fig. 4. The freely moving pendulum setup consists of two key elements: the test plate model with a dimension of 669 mm × 351 mm × 9 mm (item 4 in Fig. 4) and the test frame which is suspended above the wind tunnel floor from four cables and allows

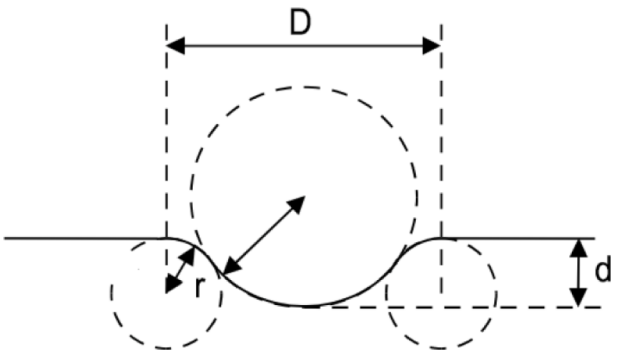

Fig. 2. Cross-section of the dimple geometry. The depth is greatly amplified for clarity. *Source:* Reprinted by permission from Springer Nature Customer Service Centre GmbH: Springer Nature, Experiments in Fluids (van Nesselrooij et al., 2016).

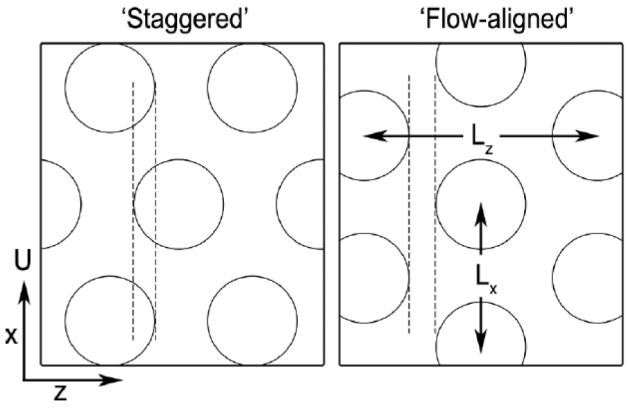

Fig. 3. Sketch of a staggered and flow-aligned pattern and the definition of streamwise and spanwise spacing (L_x, L_z).
Source: Reprinted by permission from Springer Nature Customer Service Centre GmbH: Springer Nature, Experiments in Fluids (van Nesselrooij et al., 2016).

Table 1
Summary of the parameters describing the wind tunnel plate models. All dimensions in mm.

Plate	D	d	r	L_x	L_z	Pattern
A	20	0.5	10	57.18	33.00	Staggered
B	20	0.5	10	33.00	57.18	Flow-aligned
C	20	0.5	10	34.78	20.06	Staggered
D	60	1.5	30	104.34	60.18	Staggered
E	20	1.0	10	57.18	33.00	Staggered
F	20	1.0	10	34.78	20.06	Staggered
G	60	3.0	30	104.34	60.18	Staggered

the test plate model to swing with minimal drag (item 2 in Fig. 4). The test plate model is connected through the suspended test frame to a ± 2 *N* force sensor (item 7 in Fig. 4).

There are two notable differences between the rebuilt setup used in the present study and the experiments from 2016. Firstly, the plate models had to be manufactured again. Care was taken to mill the plate models from the same material and with the same machine. All other parts of the setup were the same components that have been used in the original study. Secondly, a novel rear flow guide (item 5 in Fig. 4) has been fitted with 30 pressure taps. In the original study, only one pressure tap had been fitted in the geometrical center of the rear flow guide.

This pressure tap was utilized to measure the pressure between the rear flow guide (item 5 in Fig. 4) and the suspended test frame (item 2 in Fig. 4) and correct for the pressure differential between measurements. The additional pressure taps have been included since van Nesselrooij et al. (2022) showed the significance of the pressure correction given the expected subtle changes in drag. Pressure recordings were performed by means of an in-house developed pressure transducer (range of ±600 Pa) with a frequency of 2000 Hz and a measurement time of 5 s. Fig. 5 depicts the organization of the pressure taps. It is not expected that the differences between the original 2016 setup and the setup as utilized in the present study will affect the drag measurements. Only plate model A and the reference flat plate have been manufactured for this experiment since plate model A is the main object of interest.

Table 2
Grid spacing compared with guideline ranges for LES and DNS as provided by Bannier et al. (2015). Values are computed at the wall and at $x/\delta_{99} = 0$.

	Δx^+	Δy^+_{wall}	Δz^+
LES guideline range	30 – 60	0.3 – 1	12 – 25
Current LES	18	0.7	9
DNS guideline range	6 – 12	0.3 – 1	3 – 6

2.2. Numerical methodology

For the numerical study, the geometry of plate model A and a flat reference case are considered, using the numerical setup as described in the next sections.

2.2.1. Methods

Wall-resolved large eddy simulations (LES) of the incompressible spatially developing turbulent boundary layer flows over the flat and dimpled plates were performed with the finite-volume solver INC (Hickel and Adams, 2008; Hickel et al., 2014). The spatial discretization is based on the simplified adaptive local deconvolution method (Hickel et al., 2006; Hickel and Adams, 2007). Time-marching is performed using a third-order explicit Runge–Kutta scheme (Shu, 1988) with a time-step size corresponding to a Courant–Friedrichs–Lewy condition of one. INCA uses block-Cartesian grids to accommodate local resolution requirements and immersed boundary methods (IBM) for representing arbitrary geometries (Meyer et al., 2010).

2.2.2. Domain and discretization

The computational domain is depicted in Fig. 6. Differently from Spalart et al. (2019), a spatially developing flow is simulated to avoid uncertainties that would result from the effect of the streamwise periodic boundary conditions used in their study. Turbulent inflow data is generated with the rescaling–recycling method, see Section 2.2.3. The static pressure is fixed at the outlet and periodic boundary conditions are imposed in the spanwise direction. The no-slip condition is imposed on the lower boundary and a decay condition is imposed on the upper boundary (Hickel and Adams, 2008).

Although we refer to the current simulation as LES rather than DNS, the mesh resolution, see Table 2, is close to what is considered sufficient for DNS. Nevertheless, a subgrid-scale model is applied to account for any unresolved small-scale turbulent activity. Hyperbolic grid refinement is applied towards the wall to ensure sufficient resolution in the wall-normal direction while the grid is equidistantly spaced along the other two axes. After the transient flow structures have washed out of the domain, statistical data is collected every 50 time steps over 140 δ_{99}/U.

2.2.3. Turbulent boundary layer inflow

This study considers an incompressible zero-pressure gradient turbulent boundary layer. The turbulent inflow conditions are generated using a rescaling–recycling method (Lund et al., 1998). The inflow condition at the inflow plane (the domain inlet located at $x/\delta_{99} = -12$) consists of profiles for mean and fluctuating flow quantities. The

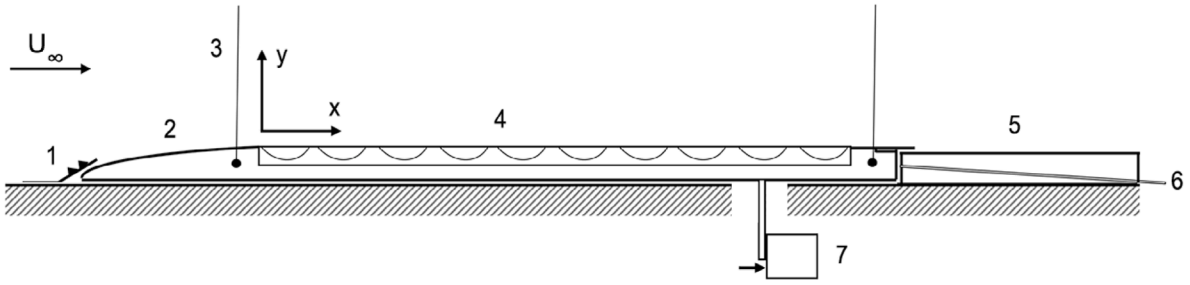

Fig. 4. Schematic view of the side of the drag measurement setup by van Nesselrooij et al. (2016). Deflector with carborundum roughness elements (1), suspended test frame (2), pendulum cable (3), test plate (4), rear flow guide (5), pressure probe (6), and force sensor (7).
Source: Reprinted by permission from Springer Nature Customer Service Centre GmbH: Springer Nature, Experiments in Fluids (van Nesselrooij et al., 2016).

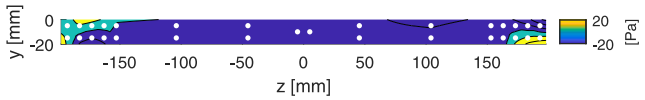

Fig. 5. Organization of the pressure taps in the rear flow guide for the replication of the setup of van Nesselrooij et al. (2016). Includes pressure data from one of the measurements as an example. Pressure is referenced against the static pressure in the wind tunnel test section.

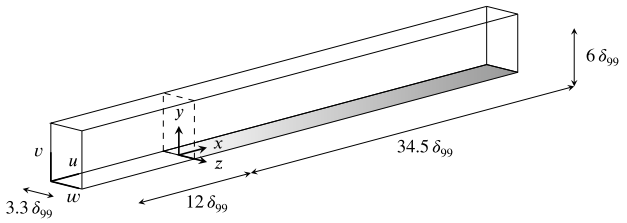

Fig. 6. Illustration of the computational domain. The dotted lines indicate the end of the developing region and the gray area indicates the flat reference geometry. δ_{99} indicates the boundary layer thickness at the inflow plane.

mean profile is based on the DNS data from Spalart (1988) while the fluctuations at a downstream plane (i.e., the source plane) in the domain are rescaled and then recycled upstream to form the turbulent inflow conditions. The region from x/δ_{99} = -12 until 0 is considered as an inflow buffer, that decouples the inflow generator from any possible effects of the dimpled surface that starts at x/δ_{99} = 0. In the inflow developing region, the recycled profiles are developing and hence the data from this region will be discarded. The Reynolds number based on δ_{99} is set to match the flow conditions of the experiments from van Nesselrooij et al. (2016) and van Campenhout et al. (2018) and equals 16,500 at the domain inlet. As such, after the inflow development region, the inflow Reynolds number based on δ_{99} is ~20,000. With an inlet δ_{99} of approximately 10 mm, the freestream velocity is U = 24.7 m/s at the domain inlet. The inflow turbulent intensity is set to 0.7% to match the experiments.

3. Experimental results

This section summarizes the results of the wind tunnel experiments. Firstly, the results obtained with the novel setup of van Nesselrooij et al. (2022) are described. For these measurements, three separate sweeps of increasing freestream velocity have been performed for plate models A to G. Before and after each measurement of a plate model, a reference flat plate measurement is performed. The final drag data of the plate model is depicted relative to the average of those flat plate measurements and is defined as ΔC_D. The boundary layer characterization for the setup has been described in van Nesselrooij et al. (2022).

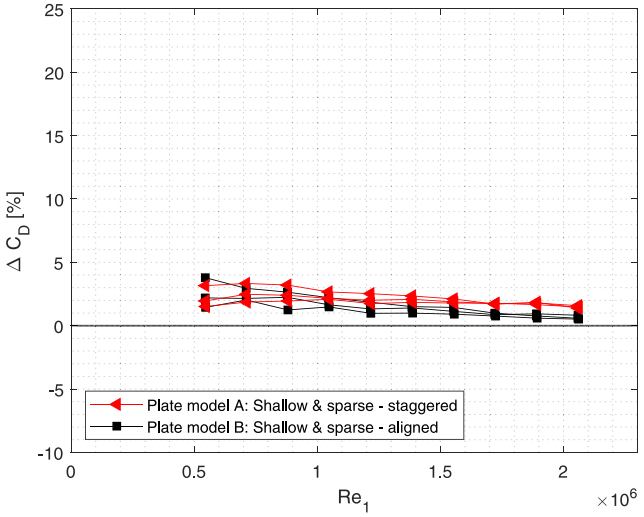

Fig. 7. Drag results for the shallow & sparse - staggered (plate model A) and shallow & staggered - aligned (plate model B) configurations relative to the flat plate. Plate model A reduced the drag in the original study by van Nesselrooij et al. (2016) while it increased the drag in the later study by Spalart et al. (2019).

Fig. 7 depicts the drag results for configurations A and B, which have the same dimple geometry and spacing as indicated in Table 1. The only difference is that plate model A has a staggered configuration while plate model B has a flow-aligned configuration, see Fig. 3. The unit Reynolds number, Re_1, is based on the freestream flow velocity and a unit length scale of one meter. The different curves reflect the different data sets obtained for each geometry. The results of configuration B are in agreement with those of van Nesselrooij et al. (2016). On the other hand, the results from configuration A do not match the 2016 study. The current measurements depict a drag increase of around 1%–2% for the entire Reynolds regime, whereas the 2016 study found a ~4% drag reduction. Furthermore, there is no clear Reynolds number dependence, which contradicts one of the main findings from the 2016 study. The results for plate model A do however align with the experimental and numerical results presented by Spalart et al. (2019), see also Fig. 10.

Fig. 8 portrays the drag results for the shallow and densely-spaced dimples, plate models C and D (see Table 1) and Fig. 9 depicts the results for the deep dimples (E to G). Note that "shallow" and "deep" refer to the depth of the dimple relative to its diameter, being 2.5% and 5% for the shallow and deep dimples, respectively. Plate models C to G all increase the drag. These findings align with the results of van Nesselrooij et al. (2016). The drag results from the densely-spaced large dimples, plate models D and G, depict that the drag decreases as the Reynolds number increases, as can be observed from Figs. 8 and 9. However, a physical explanation for this trend cannot be provided

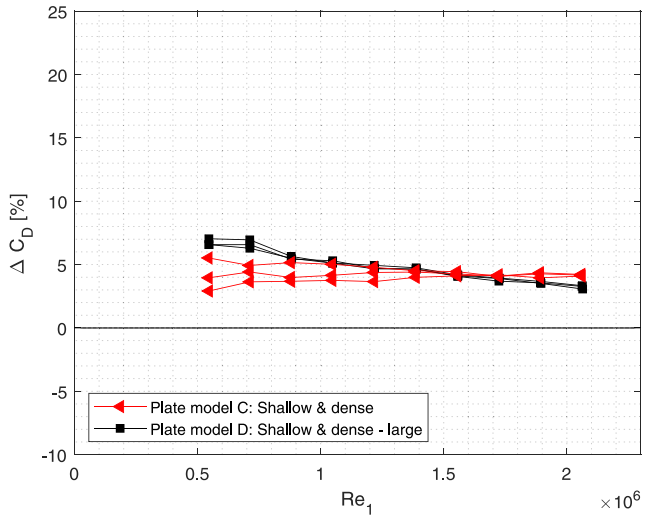

Fig. 8. Drag results for the shallow & dense (plate model C) and shallow & dense - large (plate model D) configurations relative to a flat plate.

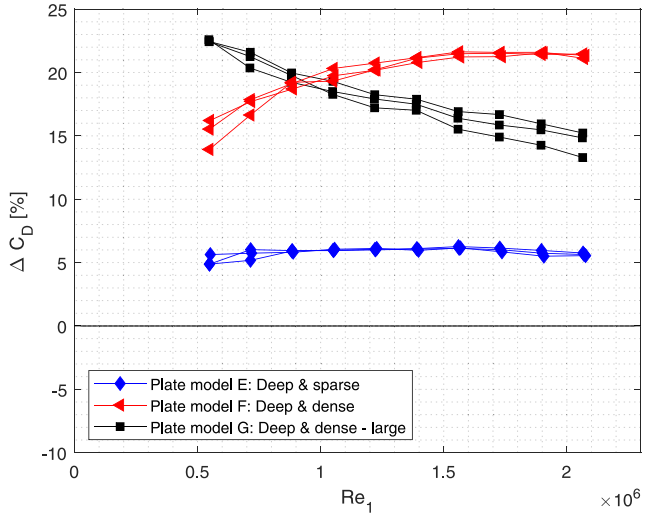

Fig. 9. Drag results for the deep & sparse (plate model E), deep & dense (plate model F), and deep & dense - large (plate model G) configurations relative to a flat plate.

based on the data and analysis presented in this article. The drag results from the current study (for each configuration averaged over the entire data set) are compared against the original 2016 study in Fig. 10. Except for plate model B, there is a consistent underestimation of ΔC_D in the 2016 study when compared to the data from the current study. Six out of seven plate models show a lower ΔC_D in the 2016 study compared to this study, with an average discrepancy of ~3%.

The results of the drag measurements from the rebuilt 2016 setup are depicted in Fig. 11. Similar to the other experiments in this study, three separate velocity sweeps with increasing freestream velocity have been performed for each dimple plate model. Before and after each dimple plate model measurement, a reference flat plate measurement is performed for reference. The drag data of the plate model is subsequently expressed relative to the average of these two flat plate measurements.

Two different data processing approaches regarding the pressure correction of the drag data were employed and the differences between these two approaches are depicted in Fig. 11. Firstly, the same pressure-correction approach as employed by van Nesselrooij et al. (2016) is considered. In this approach, only the pressure data from the two pressure taps closest to the geometrical center of the rear flow guide

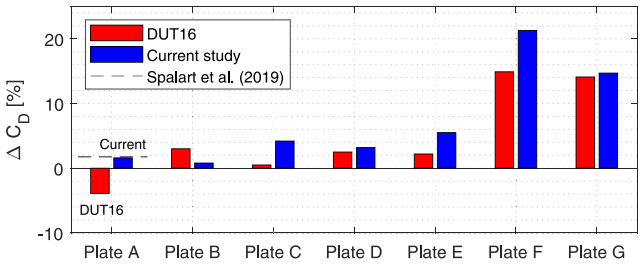

Fig. 10. Comparison between van Nesselrooij et al. (2016) (denoted as DUT16) and the current study at $Re_1 = 2 \times 10^6$. The dashed line indicates the results from Spalart et al. (2019) for plate model A.

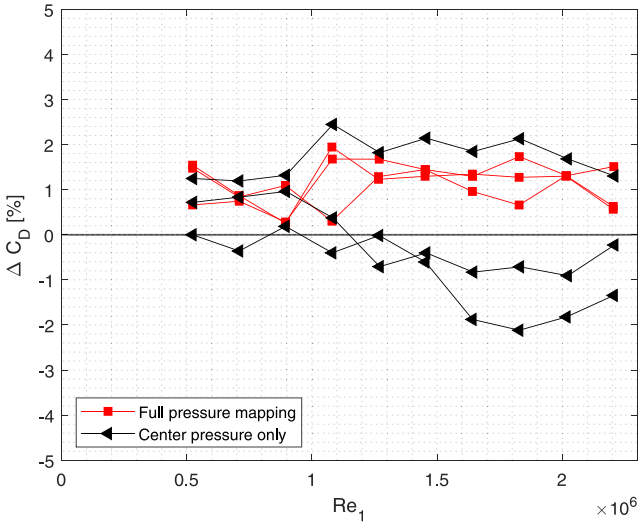

Fig. 11. Drag results for the shallow & sparse - staggered (plate model A) configuration relative to a flat plate by utilizing the rebuilt setup from van Nesselrooij et al. (2016). Final results based on the data of all 30 pressure taps as well as from only the two pressure taps closest to the geometrical center of the rear flow guide.

is taken into account. Based on this pressure data and the area of the trailing edge face, a correction is applied to the force sensor data. In the second correction approach, pressure data from all 30 pressure taps, see Fig. 5, is utilized and combined with the area of the trailing edge face in calculating the correction. Thus, the second approach has a higher spatial resolution in capturing pressure variations between the suspended test setup and the rear flow guide.

Fig. 11 shows significant differences between the results obtained with the two data processing approaches. When the data from all 30 pressure taps is considered, a drag increase of around 1%–2% is found for plate model A relative to the flat plate. This agrees with the results depicted in Fig. 7 and the results from Spalart et al. (2019). However, when only the data from the two center pressure taps is utilized, the results yield a mean drag reduction of 0.5% at the highest considered Reynolds number. Furthermore, the repeatability of the measurements deteriorates as can be seen from the relatively large spread between the individual measurements (see Fig. 11). Lastly, a trend can be observed in the data since the drag reduction increases with increasing Reynolds number. The spread between the individual measurements and the Reynolds number dependence of the drag reduction are due to a non-uniform distribution of the pressure at the trailing edge of the suspended test frame, as depicted in Fig. 5. This non-uniform distribution varies slightly between individual measurements and is not captured by the approach in which only the pressure data from the two pressure taps closest to the geometrical center of the rear flow guide is taken into account. Even though the results from the original 2016 study have not been fully replicated in this study, a drag reduction and

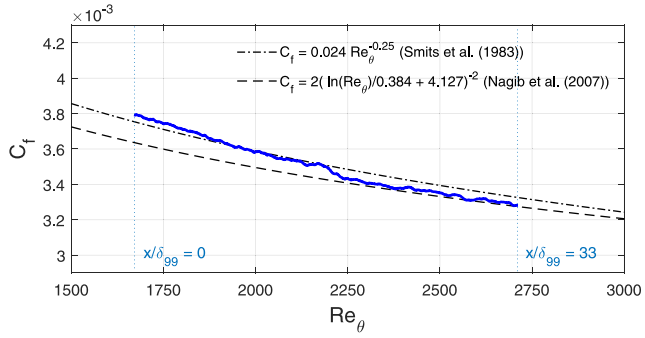

Fig. 12. Streamwise evolution of the spanwise-averaged skin friction coefficient as a function of Re_θ for the flat reference case including correlations by Nagib et al. (2007) and Smits et al. (1983).

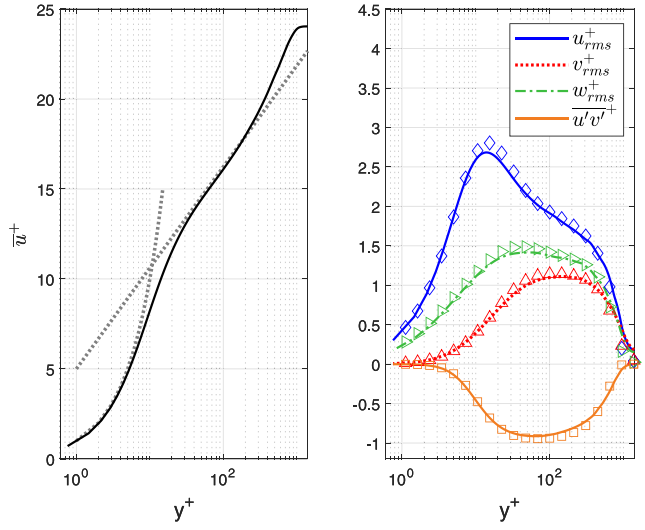

Fig. 13. Boundary layer velocity profiles for the flat reference case in inner scaling at $Re_\theta = 2313$ averaged over the region from $x/\delta_{99} = 20.4$ until 22.5 (which corresponds to the virtual location of 4th center dimple). Left: $\overline{u}^+$ (black, solid). The gray dotted lines indicate the viscous sublayer, $u^+ = y^+$, and the logarithmic region, $u^+ = \frac{1}{0.41} log(y^+) + 5.0$. Right: u^+_{rms} (blue, solid), v^+_{rms} (red, dotted), w^+_{rms} (green, dot-dashed), and $\overline{u'v'}^+$ (orange, solid). Includes reference data by Schlatter and Örlü (2010) at $Re_\theta = 2540$ as markers. (For interpretation of the references to color in this figure legend, the reader is referred to the web version of this article.)

a Reynolds number dependence are observed in both this study and the one by van Nesselrooij et al. (2016).

4. Numerical results

To assess the validity of the numerical simulation, the skin friction coefficient, C_f, for the flat reference case is depicted as a function of the Reynolds number based on the momentum layer thickness and the freestream flow velocity, Re_θ, in Fig. 12 and compared to established literature data. The skin friction coefficient is found to be in close agreement with the correlations of Nagib et al. (2007) and Smits et al. (1983). The mean velocity and Reynolds stress profiles, shown in Fig. 13 , match reference data of Schlatter and Örlü (2010).

Fig. 14 depicts the boundary layer velocity profiles for the dimpled surface as averaged over the 4th center dimple region (located from $x/\delta_{99} = 20.4$ until 22.5) compared to the flat reference case. Each case is normalized with the corresponding viscous stress. As can be observed from Fig. 14, the normalized Reynolds stresses and turbulence intensity increase over the dimpled surface. This effect is observed for every dimple within the computational domain. This increase is most pronounced in the buffer layer, whereas the viscous sublayer only

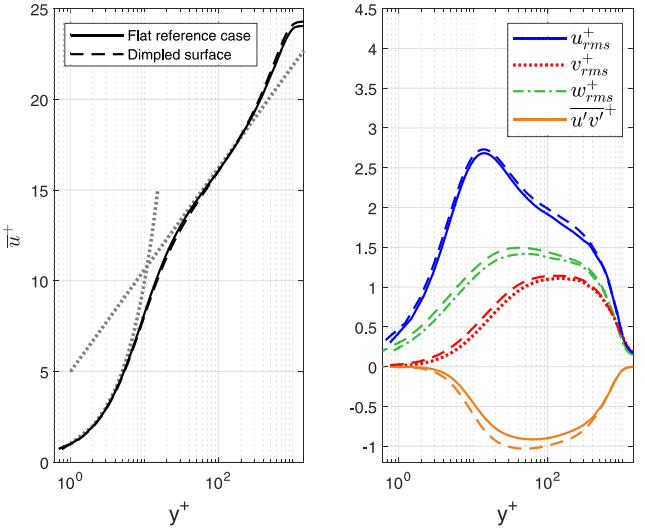

Fig. 14. Boundary layer velocity profiles for the flat reference case versus the dimpled surface (dashed lines) in inner scaling averaged over the region from $x/\delta_{99} = 20.4$ until 22.5 (which corresponds to the virtual location of 4th center dimple). Left: $\overline{u}^+$ (black, solid). The gray dotted lines indicate the viscous sublayer, $u^+ = y^+$, and the logarithmic region, $u^+ = \frac{1}{0.41} log(y^+) + 5.0$. Right: u^+_{rms} (blue, solid), v^+_{rms} (red, dotted), w^+_{rms} (green, dot-dashed), and $\overline{u'v'}^+$ (orange, solid). (For interpretation of the references to color in this figure legend, the reader is referred to the web version of this article.)

shows a minimal increase in intensity. The influence of the dimpled surface is mainly visible in the inner layer and appears negligible in the outer layer.

The spanwise mean flow velocity over the dimpled surface (plate model A) at $y/\delta_{99} = 0.05$ is depicted in Fig. 15-a. The converging–diverging flow pattern as can be observed from the spanwise velocity component distribution in Fig. 15, has been denoted "Stage 1 flow" by Tay et al. (2014). The order of magnitude of the spanwise velocity matches the literature at around 3% of the freestream flow velocity. In line with the particle image velocimetry (PIV) measurements of van Campenhout et al. (2016), the current results suggest that the mean spanwise velocity pattern in the downstream half of the dimple is stronger than in the upstream half.

The drag results for the dimpled surface and the flat reference case are depicted in Fig. 15-b to e. A higher pressure drag coefficient, $C_{d,pressure}$, is observed at the leading edge of the dimple. When the flow passes over the upstream half of the dimple, a lower pressure drag is observed. The downstream half of the dimple experiences a higher pressure drag while the pressure drag is again lower at the trailing edge of the dimple. Skin friction drag (Fig. 15-c) is lower in the upstream half of the dimple compared to the downstream half. As a result of flow acceleration/deceleration effects, the flat area upstream of each dimple experiences larger skin friction compared to the flat area downstream of each dimple. The local drag coefficient difference, ΔC_d, depicts an increase of the drag at the leading edge of the dimple, a decrease of the drag in the upstream half, and an increase of the drag in the downstream half (Fig. 15-e).

The total drag coefficient, C_d, is presented in Fig. 16. An increase in the cumulative pressure drag is observed over the dimpled surface, while the skin friction remains similar to the flat reference case. Overall, a 2% total drag increase is observed for the dimpled surface (plate model A). This finding is aligned with the numerical results of Spalart et al. (2019).

5. Discussion

The experimental and numerical results from this study are summarized in Fig. 17 alongside the results from van Nesselrooij et al. (2016), van Campenhout et al. (2018), and Spalart et al. (2019).

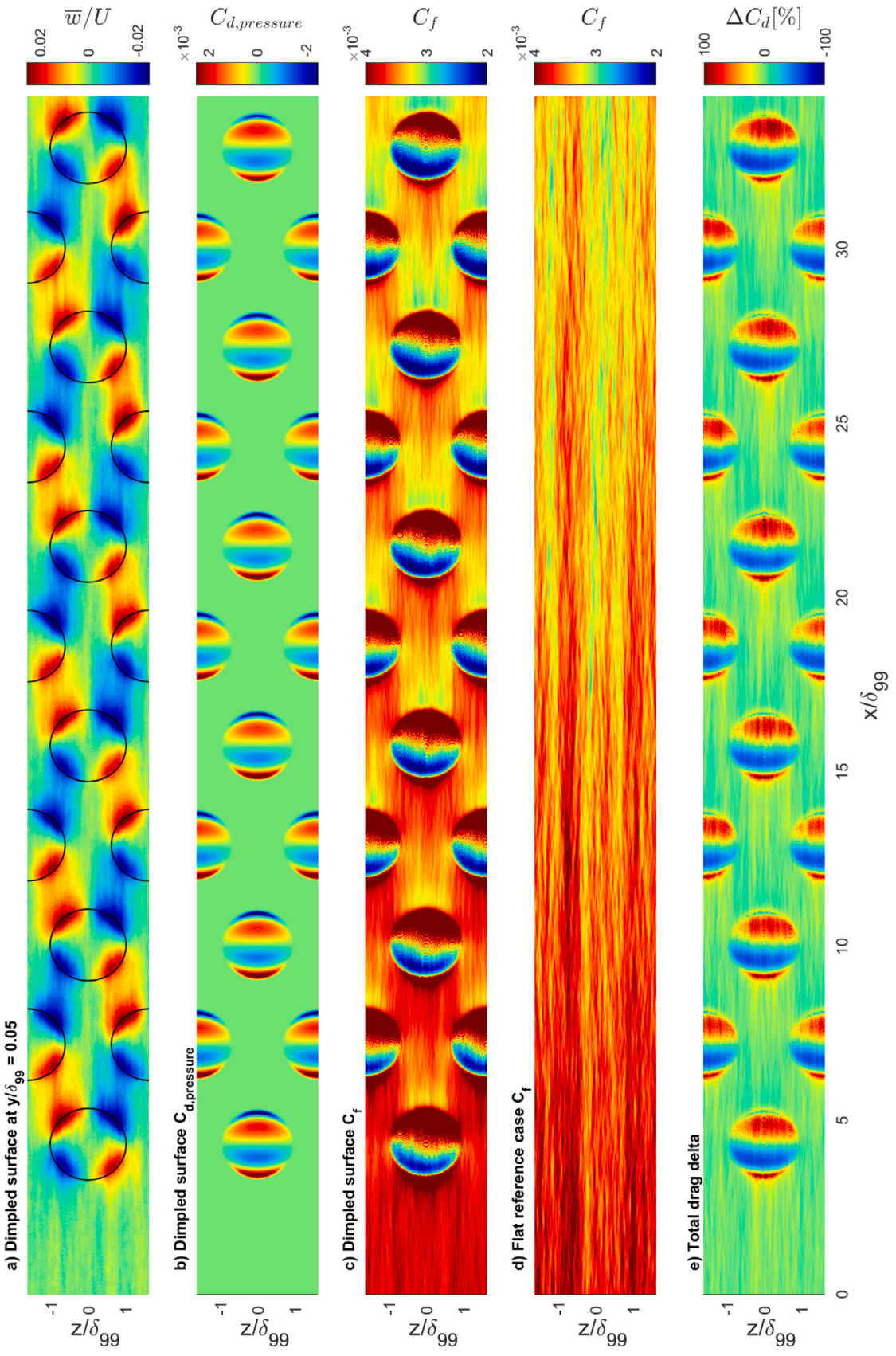

Fig. 15. Top-view of spanwise mean flow velocity over the dimpled surface (plate model A) at $y/\delta_{99} = 0.05$, where δ_{99} indicates the boundary layer thickness at the inflow plane (a), pressure drag coefficient over the dimpled surface (b), skin friction coefficient over the dimpled surface (c), skin friction coefficient for the flat reference case (d), and local drag coefficient difference between the dimpled surface and the flat reference case (e).

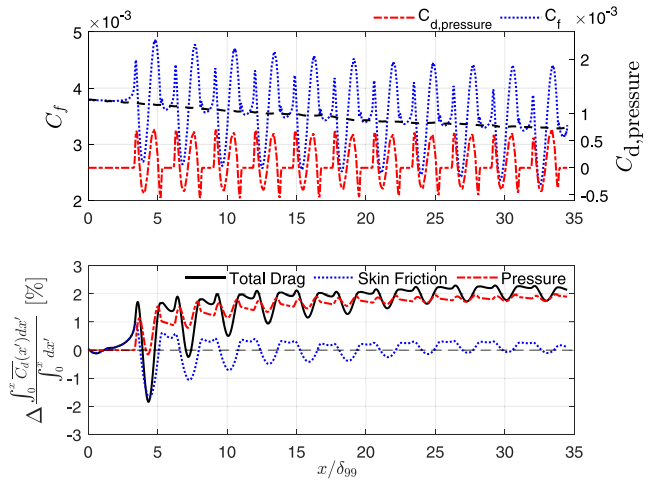

Fig. 16. Spanwise-averaged total drag decomposition (top) and the cumulative streamwise drag (below) of the dimpled surface versus the flat reference case (dashed). In the total drag decomposition (top), the left y-axis is the skin friction coefficient and the right axis is the pressure drag coefficient.

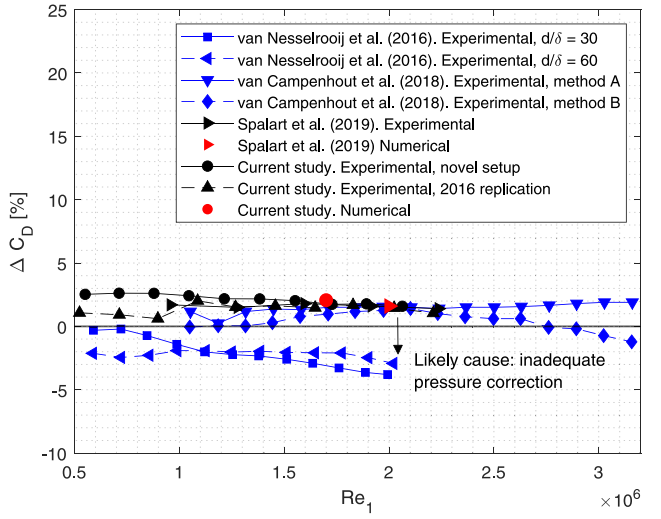

Fig. 17. Drag results from this study for the shallow & sparse - staggered configuration (plate model A) compared to data by van Nesselrooij et al. (2016), van Campenhout et al. (2018), and Spalart et al. (2019). Data from van Nesselrooij et al. (2016) depicts every second data point.

Although different methods have been used in these studies, all results have been obtained over the same dimple geometry, denoted as plate model A in this study. As can be observed from Fig. 17, the results from the current study align well with the results of van Campenhout et al. (2018) and Spalart et al. (2019). Most studies find a small drag increase of 1%–2% for all Reynolds numbers.

Results of van Nesselrooij et al. (2016) show a drag reduction. However, a replication of those 2016 experiments considered in the present study has revealed that a deficiency in the pressure force correction could have caused these discrepancies. When a more complete pressure mapping was applied, the results from the 2016 setup in this study also indicate a marginal drag increase, similar as for the other studies. The particular impact of the pressure correction on the drag measurements is evident in Fig. 11.

Although the results from the original study by van Nesselrooij et al. (2016) were not fully reproduced, we believe that an inadequate pressure mapping has been the source of the previously measured drag reductions. This conjecture is further supported by the finding in Fig. 10, where a consistent underestimation of the drag is observed. This underestimation points towards a consistent bias in either the novel setup by van Nesselrooij et al. (2022) or the setup from the original 2016 study. Given the scrutinous validation sequence that the novel setup has undergone, it is concluded that the original setup underestimates the drag due to the limited pressure mapping between the rear flow guide and the suspended test frame.

6. Concluding remarks and outlook

Regarding the drag-reducing potential of the particular dimple configuration, considered here and in previous publications, Spalart et al. (2019) have argued that "the situation is unsettled". With the data and analysis provided in the present article, we believe, that the situation can now be considered as settled. As the current results and collected literature now show, the main dimple geometry from this study (i.e., plate model A) increases the drag by 1%–2%. The variation between the results by van Nesselrooij et al. (2016) and Spalart et al. (2019) has likely occurred due to an inadequate correction of the pressure force at the trailing edge of the suspended test frame in the original 2016 study.

An important conclusion drawn based on the present LES results is that there is a significant difference between the impact of the pressure drag and the skin friction over the dimpled surface. An increased pressure drag of ~2% is observed over the dimpled surface, while the skin friction remains similar to the flat reference case. This finding could be further utilized to obtain a drag reduction by optimizing the balance between a skin friction reduction and an increase in pressure drag. Further research into novel wall-indentation geometries is deemed worthwhile given the potential gains for aeronautics as well as for other industries. An example of such novel geometries is provided by Ghebali et al. (2017), who proposed a skewed wavy wall that forces the flow in the spanwise direction. Furthermore, novel geometries could be designed in such a way that they specifically target the large-scale eddies in the boundary layer in line with the novel energy-efficient pathway as proposed by Marusic et al. (2021).

While the proposal of skewed wavy walls by Ghebali et al. (2017) and the energy-efficient pathway proposed by Marusic et al. (2021) offer promising avenues for performance improvement, the significance of these approaches in real-world conditions should be carefully considered. If the drag reduction achieved through such geometries may be limited to within 1 or 2 percent under laboratory conditions, it may be more practical to focus on other methods for reducing skin friction, given the non-ideal conditions in the real world.

As demonstrated in this article, flat plate drag measurements are notoriously challenging given the small forces involved at the conditions at which these studies are typically performed. Therefore, such measurements need to be performed with great care. The presented validation across separate research groups and a combination of experimental and numerical methods has proven its value in settling the uncertainty regarding the dimpled surface drag performance, as well as providing fundamental insight into the physical background of the phenomenon under study. More frequent use of this combined approach is strongly encouraged for future turbulent drag reduction research.

CRediT authorship contribution statement

O.W.G. van Campenhout: Conceptualization, Investigation, Writing – original draft. **M. van Nesselrooij:** Conceptualization, Methodology, Writing – review & editing. **Y.Y. Lin:** Formal analysis, Software, Writing – review & editing. **J. Casacuberta:** Methodology, Supervision, Writing – review & editing. **B.W. van Oudheusden:** Conceptualization, Supervision, Writing – review & editing. **S. Hickel:** Methodology, Supervision, Writing – review & editing.

Declaration of competing interest

The authors declare the following financial interests/personal relationships which may be considered as potential competing interests: Olaf van Campenhout reports financial support and equipment, drugs, or supplies were provided by Dimple Aerospace B.V. Olaf van Campenhout and Michiel van Nesselrooij reports a relationship with Dimple Aerospace B.V. that includes: employment and equity or stocks. Olaf van Campenhout and Michiel van Nesselrooij has patent BODY PROVIDED WITH A SUPERFICIAL AREA ADAPTED TO REDUCE DRAG issued to Dimple IP B.V. Olaf van Campenhout and Michiel van Nesselrooij has patent FLUID DRAG MEASURING METHOD AND DEVICE pending to Dimple IP B.V.

Data availability

All data that support the findings of this study are included within the article.

Acknowledgments

This work made use of the Dutch national e-infrastructure with the support of the SURF Cooperative, The Netherlands using grant no. EINF-2825. Experimental resources have been provided by Dimple Aerospace B.V. We kindly thank Dr. Modesti for assisting in the numerical simulations and N.P.J. Verdegaal for his support during the wind tunnel measurements.

References

Bannier, A., Garnier, É., Sagaut, P., 2015. Riblet flow model based on an extended FIK identity. Flow Turbul. Combust. 95 (2), 351–376. http://dx.doi.org/10.1007/s10494-015-9624-2.

Gattere, F., Chiarini, A., Quadrio, M., 2022. Dimples for skin-friction drag reduction: Status and perspectives. Fluids 7 (7), 240. http://dx.doi.org/10.3390/fluids7070240.

Ghebali, S., Chernyshenko, S.I., Leschziner, M.A., 2017. Can large-scale oblique undulations on a solid wall reduce the turbulent drag? Phys. Fluids 29 (10), 105102. http://dx.doi.org/10.1063/1.5003617.

Hickel, S., Adams, N.A., 2007. Efficient implementation of nonlinear deconvolution methods for implicit large-eddy simulation. In: High Performance Computing in Science and Engineering'06. Springer, pp. 293–306. http://dx.doi.org/10.1007/978-3-540-36183-1_21.

Hickel, S., Adams, N.A., 2008. Implicit LES applied to zero-pressure-gradient and adverse-pressure-gradient boundary-layer turbulence. Int. J. Heat Fluid Flow 29 (3), 626–639. http://dx.doi.org/10.1016/j.ijheatfluidflow.2008.03.008.

Hickel, S., Adams, N.A., Domaradzki, J.A., 2006. An adaptive local deconvolution method for implicit LES. J. Comput. Phys. 213 (1), 413–436. http://dx.doi.org/10.1016/j.jcp.2005.08.017.

Hickel, S., Egerer, C.P., Larsson, J., 2014. Subgrid-scale modeling for implicit large eddy simulation of compressible flows and shock-turbulence interaction. Phys. Fluids 26 (10), 106101. http://dx.doi.org/10.1063/1.4898641.

Kiknadze, G.I., Krasnov, Y.K., Chushkin, Y.V., 1984. Investigation of the Enhancement of Heat Transfer Due to Self-Organization of Ordered Dynamic Twisted Heat-Carrier Structures on a Heat-Transfer Surface. Technical Report, Report IV Kurchatov Institute of Atomic Energy.

Lienhart, H., Breuer, M., Köksoy, C., 2008. Drag reduction by dimples? A complementary experimental/numerical investigation. Int. J. Heat Fluid Flow 29 (3), 783–791. http://dx.doi.org/10.1016/j.ijheatfluidflow.2008.02.001.

Lund, T.S., Wu, X., Squires, K.D., 1998. Generation of turbulent inflow data for spatially-developing boundary layer simulations. J. Comput. Phys. 140 (2), 233–258. http://dx.doi.org/10.1006/jcph.1998.5882.

Marusic, I., Chandran, D., Rouhi, A., Fu, M.K., Wine, D., Holloway, B., Chung, D., Smits, A.J., 2021. An energy-efficient pathway to turbulent drag reduction. Nature Commun. 12 (1), 1–8. http://dx.doi.org/10.1038/s41467-021-26128-8.

Meyer, M., Devesa, A., Hickel, S., Hu, X.Y., Adams, N.A., 2010. A conservative immersed interface method for large-eddy simulation of incompressible flows. J. Comput. Phys. 229 (18), 6300–6317. http://dx.doi.org/10.1016/j.jcp.2010.04.040.

Nagib, H.M., Chauhan, K.A., Monkewitz, P.A., 2007. Approach to an asymptotic state for zero pressure gradient turbulent boundary layers. Phil. Trans. R. Soc. A 365 (1852), 755–770. http://dx.doi.org/10.1098/rsta.2006.1948.

Razzak, M.A., Cui, Y.D., Tay, J., Teo, Z.W., Nadesan, T., Khoo, B.C., Nguyen, V.-T., Wise, D.J., E Chua, K.T., VBL, B., 2022. Experimental study of skin friction drag reduction of turbulent boundary layer over shallow dimples. In: AIAA SCITECH 2022 Forum. p. 0712. http://dx.doi.org/10.2514/6.2022-0712.

Schlatter, P., Örlü, R., 2010. Assessment of direct numerical simulation data of turbulent boundary layers. J. Fluid Mech. 659, 116–126. http://dx.doi.org/10.1017/S0022112010003113.

Shu, C.-W., 1988. Total-variation-diminishing time discretizations. SIAM J. Sci. Stat. Comput. 9 (6), 1073–1084. http://dx.doi.org/10.1137/0909073.

Smits, A.J., Matheson, N., Joubert, P.N., 1983. Low-Reynolds-number turbulent boundary layers in zero and favorable pressure gradients. J. Ship Res. 27 (03), 147–157. http://dx.doi.org/10.1017/S0022112091000691.

Spalart, P.R., 1988. Direct simulation of a turbulent boundary layer up to $Re_\theta = 1410$. J. Fluid Mech. 187, 61–98. http://dx.doi.org/10.1017/S0022112088000345.

Spalart, P.R., Shur, M., Strelets, M., Travin, A., Paschal, K.B., Wilkinson, S.P., 2019. Experimental and numerical study of the turbulent boundary layer over shallow dimples. Int. J. Heat Fluid Flow 78, 108438. http://dx.doi.org/10.1016/j.ijheatfluidflow.2019.108438.

Tay, C.M.J., Chew, Y.T., Khoo, B.C., Zhao, J.B., 2014. Development of flow structures over dimples. Exp. Therm Fluid Sci. 52, 278–287. http://dx.doi.org/10.1017/S0022112088000345.

Tay, C.M.J., Khoo, B.C., Chew, Y.T., 2015. Mechanics of drag reduction by shallow dimples in channel flow. Phys. Fluids 27 (3), 035109. http://dx.doi.org/10.1016/j.expthermflusci.2013.10.001.

van Campenhout, O.W.G., van Nesselrooij, M., Veldhuis, L.L.M., van Oudheusden, B.W., Schrijer, F.F.J., 2016. Flow visualization over drag reducing dimpled surfaces in turbulent boundary layers using particle image velocimetry. In: 18th International Symposium on the Application of Laser and Imaging Techniques to Fluid Mechanics. pp. 4–7, http://resolver.tudelft.nl/uuid:0cb5c962-5ef1-4b52-bbc3-e6e4da665e22.

van Campenhout, O.W.G., van Nesselrooij, M., Veldhuis, L.L.M., van Oudheusden, B.W., Schrijer, F., 2018. An experimental investigation into the flow mechanics of dimpled surfaces in turbulent boundary layers. In: 2018 AIAA Aerospace Sciences Meeting. p. 2062. http://dx.doi.org/10.2514/6.2018-2062.

van Nesselrooij, M., van Campenhout, O.W.G., van Oudheusden, B.W., Schrijer, F.J.J., Veldhuis, L.L.M., 2022. Development of an experimental apparatus for flat plate drag measurements and considerations for such measurements. Meas. Sci. Technol. 33 (5), 055303. http://dx.doi.org/10.1088/1361-6501/ac527f.

van Nesselrooij, M., Veldhuis, L.L.M., van Oudheusden, B.W., Schrijer, F.F.J., 2016. Drag reduction by means of dimpled surfaces in turbulent boundary layers. Exp. Fluids 57 (9), 1–14. http://dx.doi.org/10.1007/s00348-016-2230-9.

Veldhuis, L.L.M., Vervoort, E., 2009. Drag effect of a dented surface in a turbulent flow. In: Proceedings of the 27th AIAA Applied Aerodynamics Conference. p. 3950. http://dx.doi.org/10.2514/6.2009-3950.

Walsh, M., 1982. Turbulent boundary layer drag reduction using riblets. In: 20th Aerospace Sciences Meeting. p. 169. http://dx.doi.org/10.2514/6.1982-169.